

One year of cyclic unrest in a hydrothermal field as a harbinger of a volcanic eruption

Olafur Flovenz (✉ ogf@isor.is)

ISOR - Iceland GeoSurev

Rongjiang Wang

Helmholtz-Centre Potsdam, GFZ German Research Center for Geosciences

Gylfi Hersir

ISOR - Iceland GeoSurev

Torsten Dahm

Helmholtz Centre Potsdam, Deutsches GeoForschungsZentrum GFZ - GFZ German Research Centre for Geosciences

Sebastian Hainzl

GFZ German Research Centre for Geosciences <https://orcid.org/0000-0002-2875-0933>

Magdalena Vassileva

Helmholtz Centre Potsdam, Deutsches GeoForschungsZentrum GFZ - GFZ German Research Centre for Geosciences

Vincent Drouin

ISOR, Iceland GeoSurvey

Sebastian Heimann

GFZ German Research Centre for Geosciences

Marius Isken

Helmholtz Centre Potsdam GFZ German Research Centre for Geosciences

Egill Gudnason

ISOR, Iceland GeoSurvey

Kristjan Augustsson

ISOR, Iceland GeoSurvey

Thorbjorg Agustsdottir

ISOR, Iceland GeoSurvey

Josef Horalek

Academy of Sciences

Mahdi Motagh

German Research Center for Geosciences (GFZ) <https://orcid.org/0000-0001-7434-3696>

Thomas Walter

Helmholtz Centre Potsdam - GFZ German Research Centre for Geosciences <https://orcid.org/0000-0002-9925-4486>

Eleonora Rivalta

GFZ - German Research Centre for Geosciences <https://orcid.org/0000-0001-8245-0504>

Philippe Jousset

Helmholtz Centre Potsdam GFZ German Research Centre for Geosciences

Charlotte Krawczyk

Helmholtz Centre Potsdam GFZ German Research Centre for Geosciences

Claus Milkereit


Helmholtz Centre Potsdam GFZ German Research Centre for Geosciences

Article

Keywords: volcanic eruption, seismology, earthquake

Posted Date: July 27th, 2021

DOI: <https://doi.org/10.21203/rs.3.rs-636186/v1>

License:  This work is licensed under a Creative Commons Attribution 4.0 International License. [Read Full License](#)

Version of Record: A version of this preprint was published at Nature Geoscience on May 2nd, 2022. See the published version at <https://doi.org/10.1038/s41561-022-00930-5>.

Abstract

One year of deformation and seismicity prior to a volcanic eruption in March 2021 at an oblique plate boundary in Iceland created a unique opportunity to study the interaction between upwelling magma and geothermal processes.

We apply poroelastic modelling to explain satellite geodetic data showing three uplift and subsidence cycles at the Svartsengi geothermal field and use gravity data to constrain the density of intruded material. We use recordings on optical cable to generate a high-resolution earthquake catalogue and developed new waveform stacking and migration methods to detect and locate 39,500 earthquakes.

The resulting model explains the geodetic, gravity, and seismic data by magmatic derived gas intruded into a horizontal sealed aquifer at 4 km depth in the roots of the geothermal field at the top of up-doming brittle-ductile boundary. The total injected volume is estimated $9.5 \cdot 10^7 \text{m}^3$ with optimal density of 840 kg/m^3 .

Our results suggest upward migration of three packages of volcanic gas along the brittle-ductile boundary from a subcrustal magmatic source 8–10 km east of the geothermal field, with important implications for the dynamics leading to the eruption.

Background

High temperature (HT) geothermal fields are associated worldwide with volcanism and fluid convection at plate boundaries and hot spots. Recent volcanic and seismic unrest at the Reykjanes Peninsula (RP) plate boundary in SW Iceland and the Svartsengi HT field (**Fig. 1**) reveals a previously unexplored cyclic interaction between tectonic spreading, magmatic reservoirs, and the detachment of supercritical magmatic fluids interacting with deep hydrothermal waters.

On January 22nd, 2020, an earthquake swarm started 3 km east of Svartsengi. Simultaneously, continuous GNSS stations showed uplift at the geothermal field close to the re-injection site¹ of the power plant, followed by subsidence. Three cycles of such inflations and deflations occurred until July 2020, always followed by continuous deflation and diminishing seismicity. A similar inflation started in August 2020 in the centre of the Krýsuvík HT field, 20 km east of Svartsengi (**Fig. 1**). In February 2021, crustal extension and an intense earthquake swarm revealed the formation of a NNE striking magmatic dyke in between the two HT fields, followed by a fissure eruption about 9 km east of Svartsengi.

The spreading axis of the Mid-Atlantic Ridge comes on land at the SW corner of the RP. There it bends into a 60 km long N70°E striking oblique plate boundary expressed by a 5-10 km wide seismic and volcanic zone, with large episodic earthquake swarms every 20-40 years² with magnitudes up to M 6, mostly on N-S trending strike-slip faults. Volcanic episodes occurred at intervals of 800-1000 years during the past 4000 years, the last one ended in 1240 AD³. Each volcanic episode might last for 1-3 centuries with occasional basaltic lava flows from N45°E trending fissures extending into the adjacent plates⁴. HT geothermal fields with reservoir temperature of 240-330°C at 1-3 km depth⁵ have formed at the intersection of the seismic zone and the main volcanic fissure swarms (**Fig.1**). One well, IDDP-2 at the Reykjanes HT field, was drilled to 4.6 km depth⁶ where bottom hole temperature is estimated to be about 600°C⁷ just beneath an underpressurized aquifer (<35 MPa) revealed by circulation loss in the water filled well during drilling.

The upper crust of the RP is close to 4.5 km thick^{8,9,10} and composed of basaltic extrusives mixed with a downward increasing occurrence of intrusives. The lower crust down to Moho at ~15 km depth is thought to be made of intrusives with no evidence of melt^{10,11,12}. The brittle-ductile boundary (BDB) below the seismic zone on the RP is generally at 6-7

km depth, doming up to 4-5 km depth below the HT fields^{13,14,46}. The estimated temperature at the BDB is 600-700°C (1,15)

The 76 MW_e power plant at the Svartsengi HT field and the Blue Lagoon Spa (**Fig. S1**) are the heart of the Geothermal Resource Park, providing electricity and hot and cold water to 25,000 residents and local industries¹⁶. The annual production is about 450 kg/s, of which about 300 kg/s are re-injected into the reservoir.

The relation of cyclic deformation and earthquake activity at two distinct HT fields at the RP plate boundary and the time lag until a distant fissure eruption broke out is unusual and previously not understood. Using a comprehensive modelling approach, we show for the first time that the detachment and ascent of magma-derived volatiles into a sealed aquifer at the BDB beneath Svartsengi HT field can explain the strong uplift and subsidence cycles and induced seismicity and can be interpreted as precursor to a coming eruption through the instability of a deep magma reservoir in the lower crust or upper mantle.

Transient deformation in the geothermal field

Analysis of twelve months of satellite InSAR time-series data (see methods) processed in both ascending and descending configuration reveals an elliptical area exceeding 80 km² affected by episodic uplift and subsidence, along with minor horizontal displacements (**Fig. 2a**). The elliptical area has a major axis of ~12 km striking N60°E and minor axis of 8.5 km. The major axis follows the orientation and main strike of the geothermal reservoir (**Fig. S1**) but deviates both from the N45°E strike of volcanic fissures and the N to NNE strike-slip faults mapped at the surface on the RP.

Three events of sharp uplift episodes were followed by gradual subsidence. The duration of the three successive uplift episodes increased while the uplift rate decreased correspondingly (**Fig. S2**). The first episode had the fastest uplift rate of 2.2 mm/day and climaxed at a maximum uplift of 66 mm after 30 days. It was followed by 18 days of subsidence, a total of less than 10 mm. The second episode had an uplift rate of 1.1 mm/day and produced an uplift of 55 mm in 48 days. It was followed by a faster subsidence episode lasting approximately 24 days with a subsidence of 16 mm. The final episode with an uplift rate of 0.5 mm/day produced a cumulative uplift of 32 mm within 60 days. On July 18th, an earthquake of magnitude M4.1 occurred near the inflation centre¹⁷. It was followed by a subsidence period visible on SAR until mid-December with an average subsidence rate of 0.2 mm/day and total subsidence of 38 mm. Overall, the cumulative total uplift observed at the centre of displacement was close to 150 mm and by December 2020 the actual uplift was reduced to 90 mm.

Modelling of inflation-deflation cycles

The deformation pattern suggests volume increase at depth. We first model the uplift with a simple point source in an elastic half-space¹⁸ to retrieve information about the location, depth and strength of the source. Inversion modelling suggests a source depth of 4.4 km. The horizontal position is stationary and varies only around 330 m between the three uplift episodes. The inferred volume change for the three uplift episodes is 4.70, 3.55 and 2.75 · 10⁶ m³, respectively, and cumulatively explains over 90% of the observed deformation. (**Fig. S3**).

To better match the elliptical shape of the uplift pattern, we also used rectangular dislocation models¹⁹. The uplift episodes can be modelled by three 10 m thick, 7-9 km long and 30-50 m narrow nearly horizontal intrusions at a depth between 3.7 – 4.4 km with an average strike of N60°E.

To explain the uplift and subsidence cycles, the time-dependent gravity anomalies and seismicity in the region, we tested a poroelastic model considering a strongly coupled diffusion and deformation process. This model suggests a thin, permeable porous aquifer layer in the depth of 4 km, embedded in a multi-layered poroelastic halfspace. The

elastic parameters are based on the velocity model used for earthquake locations (**Tab. S3**). During the three uplift episodes, the aquifer was pressurized through fluid intrusion along a N60°E trending line source where the magnitude of pressurisation was attenuated from the centre along the line by a Gauss-taper with a standard deviation of 2 km. We inverted for the inflow history over the full 12-month period of unrest, with an inflow of fluids during periods of inflation and zero inflow during periods of deflation (**Fig. 2e**). The resulting constant intrusion rates are 13.4, 8.1 and 5.1 m³/s, respectively, causing a total intrusion volume of about $9.5 \cdot 10^7$ m³. The induced deformation and stress changes related to the inflow and pore-pressure diffusion can explain the observed deformation cycles, particularly the fast subsidence following each cyclic uplift, but also the observed free-air gravity anomalies and seismicity patterns in time and space.

Implications from free-air gravity anomalies

Gravity combined with deformation data provides additional insights, as changes in gravity depend on the mass of the intruded fluids, while deformation depends on volume change. We measured gravity in four consecutive campaigns (**Tab. S1**) at 10-12 existing permanent stations along an L-shaped profile extending north and west from the centre of uplift (**Fig. S6**).

Gravity changes between the first and second campaign show a consistent free-air corrected gravity increase of 10-14 µGal around the centre of uplift (**Fig. S7, Tab. S1**). This value is used in the poroelastic modelling to distinguish the type of intruded fluids. A consistent free-air corrected gravity decrease of 4-8 µGal is observed at the uplift centre from April to October. Between October 2020 and February 2021, the free-air corrected gravity decrease continues at most stations. The maximum decrease averaged over the three closest stations at the centre was 5 µGal.

The poroelastic model explains the free air gravity changes (**Fig. 2b & Fig. S7**) provided that the density of the injected fluid at 4 km depth is close to 840 kg/m³ or smaller if fluid compressibility is large. This disqualifies magma as a direct cause of the pressure pulses at 4 km depth, and is supported by the fast subsidence, and points to the inflow of low-density material like water and/or CO₂.

Seismicity

The observed seismicity provides constraints on the unrest processes at depth. In general, earthquake rate increases where stresses are elevated, and earthquake locations constrain the geometry of the deformation source. Migrating seismicity fronts provide evidence of propagating intrusions or migration of pore pressure in aquifer systems. We followed two approaches to incorporate seismicity: 1) analysing the seismicity rate changes relative to the background activity, and 2) compiling a highly accurate earthquake catalogue during the uplift episodes.

To evaluate the background seismicity, we used the national Iceland Met Office (IMO) catalogue²⁰. Specifically, we estimated the rate changes during the deformation changes in space and time. For an estimated completeness magnitude, M_c , of 1.5, we first determined the average background rate between 2000 and 2020 on a 3D grid surrounding the deformation centre. The resulting rate changes were finally compared to model predictions based on Coulomb failure stress (CFS) changes induced by the deformation source derived from the InSAR data. Our model (**Fig.3**) explains the spatial and temporal distribution of the earthquakes as seismicity induced by fluid pressure increase in the roots of the Svartsengi HT field. This finding provides independent evidence for the geodetically constrained poroelastic aquifer model.

For a more detailed analysis of the spatiotemporal patterns during the unrest period, we created a new catalogue for 2020, using 26 seismic stations spaced up to 30 km around Svartsengi and, for the first time, integrated distributed acoustic sensing (DAS) data, from a 21 km long fibre optic telecommunication cable buried 80-90 cm below the surface from the southern tip of Reykjanes to Grindavík crossing the Svartsengi HT field²¹ (**Fig. S8**). The new catalogue covers the period from February 1st to August 30th. We developed a new waveform stacking and migration method applied to continuous data streams for the detection and localisation of the smallest earthquakes. We detected 39,500 earthquakes with magnitudes $M > -1$ and localise the majority automatically. The locations have high quality, both laterally and vertically, since the sensors and DAS cable were located directly above the uplift zone, and the azimuthal distribution of all stations was extraordinarily good.

The local seismicity during the Svartsengi uplift is very shallow. The lack of deeper earthquakes below the uplift centre supports the updoming of the BDB to a depth of 4 km (**Fig. 4b**). Interestingly, the long and narrow axis of updoming of the crustal seismicity resembles well the elliptical uplift pattern (**Fig. S9**). The new catalogue also shows that the very shallow seismicity mostly occurs at the centre of uplift and dips to lower levels outside the uplift-affected region, indicating that these earthquakes are probably induced by stresses generated by the bending of the crustal layer above the deformation source.

A new and wholistic model of the pre-volcanic processes

Our poroelastic model fits the deformation, gravity and seismic data (**Figs. 2 & 3**). It consists of a pressure and volume increase due to fluid intrusion into an aquifer at 4 km depth that diffuses with time and has density up to 840 kg/m³. These results disqualify magma as the intrusion material. Although re-injection fluid might comply with the density value, the re-injection rates are far too small to explain the volume and gravity change. Therefore, we propose the intrusion of magma-derived supercritical fluids, mainly CO₂. The temperature in the aquifer at the bottom of the Svartsengi HT field is likely to be close to 330°C prior to the intrusion but not higher than the 600°C at the BDB. To get a maximal density of 840 kg/m³ for CO₂ as intruded mass at 330°C, an absolute pressure of 180 MPa is needed²². This value exceeds the estimated 100-110 MPa lithostatic pressure at 4 km depth and can explain the uplift. Such a high overpressure may only develop if the fluid is temporarily connected to parts of the deeper crust. Considering the fluid compressibility might reduce the density estimate and the required pressure^{23,24}. Contribution of sulphuric gasses will have a similar effect. An elevated concentration of volatiles in the lower crust beneath the Svartsengi HT field is also independently confirmed by high V_p/V_s ratios in seismic tomography^{25,26}.

Our earthquake analysis shows that the BDB domes up from 6-7 km depth to 4 km depth beneath the centre of inflation, where the deformation data suggest the volume increase to occur. Measurements in the deep exploration wells IDDP-1 at the Krafla geothermal field and IDDP-2 at the Reykjanes geothermal field⁶ show that underpressurized aquifers exist near the BDB. The crust is in both cases fully elastic and the fluid pressure in the rock is hydrostatic down to the BDB.

We propose a model that fits available observations of gravity, seismicity and surface deformation, including the uplift, subsidence, occurrence and time scales (**Fig. 4 & Fig. S11**). Decompression melting of slowly rising magma occurs below the Moho²⁷ which is at 15 km depth¹⁰. Volatiles exsolved from the melting process, migrate upwards and become trapped at the BDB at ~7 km depth, generating strong overpressure, but not high enough to lift the overburden (~220 MPa). This might have triggered the earthquakes swarms late 2019. After reaching a certain limiting volume, magmatic volatiles flew upward along the BDB toward the underpressurized aquifer (< 35 MPa) at 4 km depth at the bottom of the convective HT field where they intrude the aquifer with pressure high enough to cause the uplift (>110 MPa).

The feeder channel model for the lower crust explains episodic inflow with exponentially decreasing intensity and increasing recurrence times. The exponential decay is expected for pressure-driven draining from a deep reservoir with finite volume²⁸. Cyclic transport of fluid batches through the channel is expected when a valve mechanism is present and injects accumulated CO₂ volume into the channel once the valve is opened. The first three cases the fluid batches were directed to Svartsengi HT field but the fourth one in August was directed to the Krýsuvík HT field where conditions as in Svartsengi are expected (**Figs. S10 & S11**).

Our model is consistent with the eruption that started March 19th, 2021. In contrast to violent initial phase of eruptions derived from a magma chamber, the eruption rate was gentle during the first month when it substantially increased. In our model the volatiles from the degassing magma had already detached from the initial magma batch prior to the eruption rising, from the upper mantle and trapped at the BDB where it forced a different path through the crust to the underpressurized geothermal reservoirs. From the total amount of CO₂ injected into the roots of the HT fields, we can estimate that the minimum volume of degassed magma beneath the present eruption site is of the order of 10 km³ (information sheet IS2). Consequently, the available volume of magma is neither a limiting factor for the longevity of the eruption nor the erupted volume.

In conclusion, our model explains for the first time the role and importance of high temperature geothermal fields in the complicated mechanism leading to volcanic eruptions at oblique divergent plate boundaries of the oceanic crust.

Methods

InSAR data processing

We exploited the Copernicus Sentinel-1A and 1B satellite SAR data, which are available over Iceland in ascending (08/01/ -15/12/2020) and descending (06/01 -13/12/2020) orbits with a revisit time of 6 days for each track. By calculating a single interferogram for the cumulative period between 20/01/-17/07/2020, we found four fringes in both geometries, representing a shift of approximately 11 cm in the line of sight (LOS) direction (**Fig. S4**). A more detailed InSAR time series analysis shows three inflation and deflation episodes (**Fig. S2**): first uplift 19/01 - 18/02/2020, second uplift 07/03 - 24/04/2020, and third uplift 18/05 - 17/07/2020. **Due to the 6-day revisit time of Sentinel1A/1B acquisitions the exact days of inflation/deflation episodes may be shifted by a few days.** The time-series analysis was carried out using the Small Baseline Subset (SBAS) algorithm²⁹, implemented in SARscape, which is based on the combination of interferograms characterized by small normal and temporal baselines, allowing to maximize spatial and temporal coherence and therefore the quality of the interferograms (maximum temporal baseline 18 days, multi-look of 7:2 for range and azimuth direction, Goldstein filter window size of 32 pixels, coherence threshold of 0.2, a ground resolution of 30 m). The topographic phase contribution was subtracted using the ArcticDEM digital terrain model of 2 m spatial resolution. InSAR time-series were compared to data from a GNSS station provided by the IMO and available through the University of Iceland³⁰, showing good agreement for both ascending and descending dataset (**Fig. S2 a and b**). Ascending and descending LOS displacement maps were combined to derive the vertical and the EW components of the ground motion (**Fig. S5**).

Gravity data processing

Each of the four gravity campaigns (**Fig. S6**) lasted for a few days. Elevation and gravity at the second northernmost station (HS22) were used as a reference, but free-air corrected of up to 2.6 µGal to account for small elevation changes at this site between campaigns. The gravity value at the end stations (HS16 and SNH25) were less constrained or had difficult local conditions due to snow and ice and were therefore regarded as unreliable. Finally, the gravity data were

corrected for tidal and latitude effects and free air gravity computed using elevation changes obtained from InSAR measurements. The data were not corrected for ocean tides, as these effects can be considered negligible.

The uncertainty in similar gravity campaigns is generally of the order of 10-15 μGal for individual data points. These error limits are, however, highly dependent on external conditions like weather prior to and during the measurements, the local site condition, the nearby anthropogenic activity, or seismic noise. We selected quiet and calm days to minimize the measurement uncertainty. Our dataset provides consistent maximum values close to the centre of uplift which decrease with distance. However, a few data points are outliers, both with respect to the general trend with time and the nearby stations. It is our estimate that, apart from obvious outliers and with respect to internal consistency of the data, the error limits are close to $\pm 5 \mu\text{Gal}$ at the centre of uplift.

We corrected for long term background gravity reduction caused by the net production of geothermal fluid at Svartsengi³¹. The ratio of the total gravity decrease from 1976 to 2014 to the corresponding net mass production, gives a gravity decrease of $0,67 \cdot 10^{-9} \mu\text{Gal}/\text{kg}$. By applying this to the estimated production of 2020 we get a value of 5.1 $\mu\text{Gal}/\text{year}$ at the centre of uplift.

Finally, we estimated the gravity increase during the first week of uplift in January 2020 prior to the first gravity campaign. At that time, the central uplift was already 4 cm. Computing the ratio between the free-air corrected gravity increase and total uplift between the first and the second gravity campaigns reveals 170 $\mu\text{Gal}/\text{m}$ resulting in 7 μGal gravity increase during the first week of uplift (**Tab. S1**).

Poroelastic modelling

To explain the observed surface uplift, we first tested the widely used Mogi model^{18,32} which describes a pressure increase within a spherical chamber in a homogeneous elastic half-space. The best-fit source depths are found to be 4.0, 4.4 and 4.9 km for the 3 uplift episodes, respectively. Though this simple elastic model can reproduce the cumulative surface uplift in space (**Fig. S3**), it, has several issues: 1) The subsidence motion after each uplift episode seems too fast and large to be explained by the cooling process of the intruded magma (**Fig. 2d**). 2) The induced change in Coulomb stress is concentrated directly around the assumed magma chamber and therefore cannot explain the triggered seismicity, which has been observed in a widespread area (**Fig. 3**). 3) Using a realistic estimate of magma density ($\sim 2700 \text{ kg}/\text{m}^3$), it is difficult to explain all campaign gravity satisfactorily with the episodic magma intrusions based on the deformation data. 4) Most importantly, there is no indication for the existence of a magma chamber under the Svartsengi uplift area. Actually, anomalous low V_p/V_s ratios are observed in the lower crust beneath Svartsengi^{25,26} indicating gas-saturated porous rocks rather than partial melting.

Therefore, we present a more realistic poroelastic diffusion-deformation model using the semi-analytical tool POEL³³, which simulates strongly coupled diffusion-deformation processes induced by injection tests. Based on Biot's linear poroelasticity theory, a poroelastic medium is defined usually with 5 parameters, i.e., the shear rigidity μ , the drained Poisson ratio ν , the undrained Poisson ratio ν_u , the Skempton coefficient B and the hydraulic diffusivity D . In the first step, we adopt the 1D seismic SIL reference model (**Tab. S3**)³⁴. As the diffusion effect might be negligible in the seismic frequency band, μ and ν_u can be derived simply from the density and seismic velocities given in the SIL model. Except for a thin permeable aquifer, all other layers are assumed to be nearly impermeable ($D=0.001 \text{ m}^2/\text{s}$). Additionally, we assume that the whole half-space medium is fully saturated ($B=0.99$) and has a standard drained Poisson ratio (0.25). The depth z , and poroelastic parameters ν_u and D of the aquifer layer were optimized to best fit the InSAR data. Note that the thickness of the aquifer can be fixed (here 10 m), as the surface deformation is only sensitive to the aquifer transmissivity, which is proportional to the product of thickness and hydraulic conductivity.

The source is represented by episodic fluid injection into this thin and confined aquifer. The central location of the injection coincides with the maximum surface uplift at 63.870°N/22.465°W. Each of the 3 uplift episodes is attributed to a period with constant injection rate. The timing of the 3 injection periods is estimated directly by the uplift-subsidence turning points of the InSAR time series with a resolution of 6 days, i.e., Episode 1 from day 12 to 42, Episode 2 from day 60 to 108, and Episode 3 from day 132 to 192 of year 2020. Note the surface uplift exhibits a slightly elliptic pattern, which can be interpreted reasonably by a dominant diffusion along the main strike of the Svartsengi HT field (**Fig S1**). Therefore, we use a Gaussian line source instead of a point source. The orientation and the characteristic length of the source was optimized, too. Note that the parameters of the aquifer and the source geometry have a nonlinear control on the surface deformation, while the 3 constant intrusion rates are linearly related with the surface uplift. We optimize the nonlinear parameters by a Monte Carlo search. For each set of given nonlinear parameters, we estimate the 3 intrusion rates by the least-squares method. The final best-fit model is defined by the minimum misfit. The corresponding best-fit aquifer parameters are given by $z = 4.0$ km, $v_u = 0.35$, and $D = 0.15$ m²/s. The best-fit line source has a characteristic length of 4.0 km (two sigma of Gaussian distribution) and is oriented to N60°E. The three constant intrusion rates are 13.4, 8.1 and 5.1 m³/s, respectively, causing a total intrusion volume of about $9.5 \cdot 10^7$ m³. The normalized variance of misfits to all ascending and descending InSAR datasets, each consisting of 139 images, are 4% and 10%, respectively.

For the quasi-static induced poroelastic deformation, only the volume, rather than the density, of the intruded fluid is relevant. The gravity measurements provided an independent constraint on the density of the intruded fluid. The internal deformation has no effect on the free-air gravity change for spherical pressure sources in a homogeneous half-space³⁵. Based on this, and on predictions from superposition of spherical pores³⁶, we suppose the internal deformation is a secondary effect and only consider the primary effect of the intruded mass on the free-air gravity change. For this purpose, we use the POEL output for Darcy flux to calculate the spatio-temporal redistribution of the intruded mass within the aquifer layer and its contribution to the gravity variations on the surface. A simple comparison between the predicted and observed free-air gravity anomalies yields a fluid density estimate of about 840 kg/m³. The misfits of the model to the data are all within the measurement uncertainties (**Fig. S7**).

Joint analysis of DAS and a local seismic network by waveform attribute stacking

The DAS strain-rate data have been recorded using an Silixa iDAS (version 2) interrogator with a sampling frequency of 1 kHz, a gauge length of 10 m and spatial channel offset of 4 m along the full length of the fibre. The DAS data has been included as 20 virtual single-component stations by extracting the DAS signal at regular 500 m intervals along the fibre. For each virtual station, the signal was integrated over 36 m (9 channels) along the cable to improve the signal to noise ratio.

The employed automatic detection method³⁷ is based on an image function (IF) computed for a grid of potential source positions and times. The IF is computed from the stacking of time-back-shifted waveform attributes of P- and S-phases using the local velocity model (**Tab. S3**). Waveform attributes of P-phases employ a smoothed STA/LTA function³⁸ calculated from filtered seismograms. S-phase attributes are calculated from a smoothed squared signal which is more sensitive to phases of highest amplitudes. Smoothing causes the detector to be more robust against errors in the assumed seismic velocities and reduces the computational cost. Waveform attributes are normalized by a moving average with a duration longer than the duration of a typical transient event. Seismic events appear as spatio-temporal peaks in the 4D image function. A detection is registered when the IF exceeds a certain threshold value. The position of the spatio-temporal peak is used to provide the origin time and location. The detector is implemented in the Lassie software package, distributed under the Pyrocko framework³⁹ (**Tab. S2**).

Seismicity model

Earthquake triggering is expected for positive changes of the induced CFS, while no triggering is expected for negative changes^{40,41}. For simplicity, we assume that the number of earthquakes is proportional to positive CFS-changes and consider stress shadowing (Kaiser effect) by only allowing triggering if the absolute stress exceeds all precursory values^{42,43}. Thus the predicted cumulative number of induced events becomes $N(\mathbf{x}, t) \sim \max(\text{CFS}(\mathbf{x}, \text{time} \leq t))$.

The CFS-change is given by $S(\mathbf{x}, t) = \tau_{\max}(t) + f p(\mathbf{x}, t)$, where f is the friction coefficient, τ_{\max} and p are the induced maximum shear and pore pressure, respectively, based on the poroelastic model described above. Here we use the maximum shear value to account for variable receiver mechanisms. However, we find that the results are robust if we calculate CFS for a fixed right-lateral NS strike-slip mechanism. We calculated the CFS in a spatial box with a dimension of 30 km in NS- and 60 km in EW-direction, centered at the geodetically inverted deformation source, with a grid spacing of 0.5 km and at ten depth levels from 0.5 km to 9.5 km.

The susceptibility to stress changes is assumed to be proportional to the fault density estimate, based on preceding seismicity, so-called background activity. For that purpose, we analyzed the IMO-catalog using $M \geq 1.5$ events that occurred in this region between 2000 and 2019. Note that the catalog is complete for this magnitude cutoff. The rate of $M \geq 1.5$ background events in the selected region is found to be $r = 0.76 \text{ days}^{-1}$, which translates to $r = 2.41 M \geq 1$ events days^{-1} assuming a Gutenberg-Richter magnitude distribution with $b=1$.

The epicenters are laterally smoothed using a Gaussian filter with a standard deviation of 1 km, and the depth distribution is approximated by a Gaussian distribution with a mean of 5.7 km and a standard deviation of 1.8 km. After normalization, this resulted in a probability $p_r(\mathbf{x}_i)$ for the occurrence of an event in a given 3D-grid cell \mathbf{x}_i .

The spatiotemporal rate of expected events is simply equal to $R(\mathbf{x}_i, t) = r p_r(\mathbf{x}_i) + c p_r(\mathbf{x}_i) d/\text{dt CFS}(\mathbf{x}_i, t)$ for positive stress changes and CFS exceeding its preceding maximum value and $R(\mathbf{x}_i, t) = r p_r(\mathbf{x}_i)$ else. The model has two parameters, (i) the friction coefficient f , which has typical values in the range from 0.1 to 0.8, and (ii) the susceptibility parameter c . We find that f only slightly affects the results and set it to $f=0.7$ ⁴⁴. The parameter c is set by the condition that the predicted total number of events in the space-time volume is equal to the number of observed earthquakes.

Cyclic injection model

We explain the unrest at the Svartsengi HT field by at least two interacting processes: (1) continuous, slow inflow of magma from the mantle into the base of the lower crust and (2) cyclic rise of low-density pressurized fluids to a depth of 4 km, along the updoming BDB. The low-density fluids could be magmatic volatiles such as CO_2 . The volatiles either rise from melting source at greater depths or exsolve directly from the magma that has accumulated at the BDB.

The drainage of a deep reservoir by viscous channel flow is similar to the gravity-driven outflow from a tank through a pipe. If viscosity is dominant, the flux follows an exponential decay with $q(t) = q_0 e^{-t/t_0}$, where q_0 is the initial flux at time $t=0$ with $t_0 = r^2 h_2(t=0)/q_0$ (Fig. 5A & information sheet IS1). The ascent height h or the length L of the inclined channel do not enter the problem. The modeling of the total influx after three uplift episodes leads to a draining decay time of $t_0 = 115$ days and an initial flux of $q_0 = 3.2 \text{ m}^3/\text{s}$ (Fig. 5b).

The cyclic ascent of finite-volume fluid batches can be explained by the fracture-mechanical concept of buoyancy-driven fluid ascent. The process is controlled by the filling of fluid batches with flux rate $q(t)$, their detachment from the feeding reservoir, and the ascent through a channel or fault to the outflow point at 4 km depth (injection into the sealed aquifer). The problem can be illustrated with the transport of continuously arriving packages with an “elevator system”.

Each elevator is filled to its maximum load before it departs. The volume of intrusion batches at the upper aquifer has been estimated at $\sim 34 \cdot 10^6 \text{ m}^3$, $\sim 33 \cdot 10^6 \text{ m}^3$ and $\sim 26 \cdot 10^6 \text{ m}^3$ for the first, second, and third batch, respectively (**Fig 5b**). A decrease of the batch volume can be understood from the continuous reduction of the fracture roughness of rock the more often a batch rises. If the flux of arriving packages is high, the time to load the elevator is short. If the flux continuously decreases, the loading time increases. The ascent velocity of the fluid batch is almost independent of the flux at the "filling station" and only determined by the properties of the channel and the enclosed fluid volume. A constant ascent velocity is reasonable from a fracture mechanical approach and e.g. supported by laboratory experiments of finite volume fluid ascent in gelatine ⁴⁵.

The model explains the observed time function of the accumulated, injected volumes, the onset and inter-event time of the three uplift cycles (**Fig. 5 b & c**). The fit has been obtained with the requirement that the accumulated volume at the end of phase 3, $\Sigma V = V_1 + V_2 + V_3$, and the onset of the first injection phase are explained. The model is also consistent with the onsets of the uplift phases 2 and 3, and maybe a fourth phase at Krýsuvík in September 2020 (**Fig. 5c & Figs. S10 & S11**). What the model cannot resolve is the ascent times of the fluid batch after the detachment from the reservoir to the injection point at the aquifer at 4 km depth. Therefore, all times measuring the beginning of a new uplift phase in **Fig. 5b** and **c** are arrival times of the fluid batch at 4 km depth. For instance, the start of the filling of the first fluid batch is estimated for the 18th of December 2019 (**Fig. 5c**), which correlates with the occurrence of the strong earthquake swarm from 15th- 20th of December 2019 at 5-6 km depth and about 7 km east of the centre of uplift. Therefore, we suggest that the inflow in the channel occurred at this location. This would also link the unrest beneath Svartsengi to the eruption that started in March 2021 just above the December 2019 earthquake swarms (**Fig. S9**). The increasing duration of the injection into the aquifer indicates that the pressure difference between the head of the fluid batch and the sealed aquifer is decreasing with every arrival of new over-pressurized batch. This is expected if the vertical height of the batch (its volume) decreases but may also indicate that the aquifer is more and more pressurized by the inflow of fluids. Consequently, the layer above the aquifer was uplifting and bending. Parts of the overpressure in the aquifer diffused away, but not all before the arrival of the next batch.

Declarations

Acknowledgements

The authors are grateful to all those who assisted to generate this article including Halldór Geirsson, University of Iceland, for providing the time series of a permanent GPS station, allowing us to control InSAR data, Ingvar Þór Magnússon for gravity data, Mila Telecommunication Company for access to the fiber optic cable, Iceland Met Office for the access to the earthquake catalogue and GPS stations and Christopher Wollin and Kemal Erbas for DAS assistance. The field work of GFZ was part of a HART rapid response activity funded by GFZ. DEM(s) were created from DigitalGlobe, Inc., imagery and funded under National Science Foundation awards 1043681, 1559691, and 1542736.

Author contributions:

OGF Co-ordination, writing, analysis of gravity, seismic and geothermal data, modelling concepts.

RW Numerical and theoretical modelling, development of porous media deformation approach and gravity modelling.

GPH Gravity measurements, data acquisition DAS, field work management.

TD Coordination, writing, modelling concepts, analytical model of cyclic channel flow.

- SH1 Statistical analysis and modelling of seismicity.
- MV Analysis of InSAR data, Mogi model inversion.
- VD Analysis of InSAR data.
- SH2 DAS processing, development of the Lassie stacking approach, automatic earthquake detection/location for the combined network.
- MI DAS data conversion and processing, earthquake detection/location, code development.
- EÁG Seismicity analysis, incl. focal mechanisms, data acquisition DAS, manual location of earthquakes from the enlarged network.
- KA Seismicity analysis, seismic network, contribution to field activity.
- ThÁ Seismicity analysis, incl. focal mechanisms.
- JH Contributed data from Czech temporary network.
- MM Supervision and quality control InSAR analysis at GFZ.
- TW Coordination InSAR analysis, contribution to manuscript drafting and writing.
- ER Contributon to manuscript review, internal review of channel flow and fluid transport models.
- PJ Concept DAS measurements and coordination DAS data acquisition, coordination of fieldwork in MAGIC at GFZ.
- CK Support of MAGIC HART initiative at GFZ, coordination of DAS data processing and storage.
- CM Installed temp. seismic stations, field work coordination, conversion of seismic data, coordination of analysis and writing team at GFZ.

References

1. Flóvenz, Ó. et al. The interaction of the plate boundary movement in 2020 and exploitation of geothermal fields on the Reykjanes peninsula, Iceland. *Proceedings of the World Geothermal Congress 2020+1*, (2021).
2. Björnsson, S., Einarsson, P., Hjartardóttir, Á.R. & Tulinius, H. Seismicity of the Reykjanes peninsula 1971 – 1976. *J. Volcanol. Geotherm. Res* **391**, 106369, (2020).
3. Sæmundsson, K., & Sigurgeirsson, M.Á. Reykjanesskagi. In Sólnes J. et al. (ed), Náttúruvá á Íslandi, *Viðlagatrygging Íslands/Háskólaútgáfan*, 379–401 (2013).
4. Sæmundsson, K., Jóhannesson, H., Hjartarson, Á., Kristinsson, S.G. and Sigurgeirsson, M. Geological map of Southwest Iceland, 1:100.000. *Iceland GeoSurvey*, (2010).
5. De Freitas, M.A. Numerical modelling of subsidence in geothermal reservoir: Case study of the Svartsengi geothermal system, SW-Iceland. *MSc thesis, University of Iceland*, ISBN 978-9979-68-486-2, (2018).
6. Friðleifsson, G.Ó. et al. The Iceland deep drilling project at Reykjanes: Drilling into the root zone of a black smoker analog. *J. Volcanol. Geotherm. Res* **391**, 106435, <https://doi.org/10.1016/j.jvolgeores.2018.08.013> (2020).
7. Bali, E. et al. Geothermal energy and ore-forming potential of 600 °C mid-ocean-ridge hydrothermal fluids. *Geology*, **48**, <https://doi.org/10.1130/G47791.1>, (2020).

8. Pálmason, G. Crustal structure of Iceland. *Soc. Sci. Isl., Reykjavik Iceland*, **XL**, (1971).
9. Flóvenz, Ó.G. Seismic structure of the Icelandic crust above layer three and the relation between body wave velocity and the alteration of the basaltic crust, *J. Geophys.*, **47**, 211–220, (1980).
10. Weir, N.R.W. et al. Crustal structure of the northern Reykjanes ridge and the Reykjanes peninsula, southwest Iceland. *J. Geophys. Res.*, **106**, 6347-6368, (2001).
11. Hersir, G.P. et al. Krýsuvík high temperature geothermal area in SW Iceland: Geological setting and 3D inversion of magnetotelluric (MT) resistivity data. *J. Volcanol. Geotherm. Res.* **391**, 106500, <https://doi.org/10.1016/j.jvolgeores.2018.11.021> (2020).
12. Karlsdóttir, R., Vilhjálmsson, A.M. & Guðnason, E.Á. Three dimensional inversion of magnetotelluric (MT) resistivity data from Reykjanes high temperature field in SW Iceland. *J. Volcanol. Geotherm. Res.* **391**, 106498, <https://doi.org/10.1016/j.jvolgeores.2018.11.019> (2020).
1. Blanck, H., Jousset P., Hersir, G.P., Ágústsson, K. & Flóvenz, Ó.G. Analysis of 2014–2015 on- and off-shore passive seismic data on the Reykjanes peninsula, SW Iceland. *J. Volcanol. Geotherm. Res.* **391**, 106548, <https://doi.org/10.1016/j.jvolgeores.2019.02.001> (2020).
14. Kristjánsdóttir, S. Microseismicity in the Krýsuvík geothermal field, SW Iceland, from May to October 2009, *M.Sc. thesis, Faculty of Earth Sciences, University of Iceland*, (2013).
 1. Ágústsson, K. & Flóvenz, Ó.G. The Thickness of the seismogenic crust in Iceland and its implications for geothermal systems. *Proceedings of the World Geothermal Congress 2005*. (2005).
16. Albertsson, A. & Jónsson J. The Svartsengi resource park. *Proceedings World Geothermal Congress 2010*, (2010).
17. Icelandic Meteorological Office. <https://skjalftalisa.vedur.is>
1. Mogi, K. 1958. Relations between the eruptions of various volcanoes and the deformation of ground surfaces around them. *Bull. Earthquake Res.Inst. University Tokyo*, **36**, 99-134.
19. Okada, Y. Surface deformation to shear and tensile faults in a halfspace. *Bull. Seism. Soc. Am.*, **75**, (1985).
20. Böðvarsson, R., Rögnvaldsson, S.T., Slunga, R., & Kjartansson, E. The SIL data acquisition system at present and beyond year 2000. *Phys. Earth Planet. Inter.*, **113**, 89–101. (1999).
21. Jousset, P. et al. Dynamic strain determination using fibre-optic cables allows imaging of seismological and structural features. *Nature Communications*, DOI: 10.1038/s41467-018-04860-y, (2018).
 1. Industrial Refrigeration Consortium. Fluid property calculator. <https://irc.wisc.edu/properties/>
23. Johnson, D.J., 1992. Dynamics of magma storage in the summit reservoir of Kilauea volcano, Hawaii. *J. Geophysical Res.* **97**, 1807-1820, (1992).
24. Segall, P. Earthquake and volcano deformation. Princeton University Press. 425 (2010).
 1. Geoffroy, L., & Dorbath, C. Deep downward fluid percolation driven by localized crust dilatation in Iceland. *Geophys. Res. Lett.* **35**, 117302, doi:10.1029/2008GL034514, (2008).
 2. Hobé, A., Tryggvason, A., Almqvist, B., & Gudmundsson, O. Interpreting Time-Varying Processes using Empirical Data, *EGU General Assembly 2021*, online, 19–30 Apr 2021, EGU21-9509, <https://doi.org/10.5194/egusphere-egu21-9509>, (2021).

27. Institute of Earth Sciences, University of Iceland. Characterisation of rock samples collected on the 1st and 2nd days of the eruption - major elements and mineral chemistry, http://earthice.hi.is/characterisation_rock_samples_collected_1st_and_2nd_days_eruption_geldingdalur.
28. Gudmundsson M. T. et al. Gradual caldera collapse at Bárðarbunga volcano, Iceland, regulated by lateral magma outflow. *Science*, **353** (6926), doi:10.1126/science.aaf8988. (2016)
1. Berardino, P., Fornaro, G., Lanari, R. & Sansosti, E. A new algorithm for surface deformation monitoring based on small baseline differential SAR interferograms. *IEEE Transactions on Geoscience and Remote Sensing* **40**, 2375–2383 (2002).
30. Institute of Earth Sciences, University of Iceland. https://notendur.hi.is/~hgeirs/iceland_gps/icel_400p.html
31. Orkustofnun. <https://orkustofnun.is/gogn/Talnaefni/OS-2020-T009-01.pdf>, (2020).
32. Lisowski et al., 2006. Analytical volcano deformation source models. In: *Volcano Deformation*. Springer Praxis Book, Berlin, Heidelberg. 279-304, 10.1007/7978-3-540-49302-0_8
33. Wang, R.A. & Kuempel, H.J. Efficient modelling of strongly coupled, slow deformation processes in a multilayered half-space. *Geophysics*, **68**, 705-717, (2003).
34. Stefánsson, R. et al. Earthquake prediction research in the South Iceland seismic zone and the SIL project. *Bull. Seism. Soc. Am.*, **83**, 3, 696-716, (1993).
35. Walsh, J. B., & Rice J. R. Local changes in gravity resulting from deformation, *J. Geophys. Res.*, **84**, 165 – 170, doi.org/10.1029/JB084iB01p00165, (1979).
36. Amoruso, A., and L. Crescentini. "Shape and volume change of pressurized ellipsoidal cavities from deformation and seismic data." *Journal of Geophysical Research: Solid Earth* 114.B2 <https://doi.org/10.1029/2008JB005946>, (2009).
37. Lopez Comino, J.A. et al. Characterization of Hydraulic Fractures Growth During the Aspo Hard Rock Laboratory Experiment (Sweden). *Rock Mechanics and Rock Engineering*, **50**, 11, 298-3001, (2017)
38. Allen, R.V. Automatic earthquake recognition and timing from single traces. *Bull. Seism. Soc. Am.* **68**, 1521-1532. (1978).
39. Heimann, Sebastian; et al. Pyrocko - An open-source seismology toolbox and library. V. 0.3. GFZ Data Services. <https://doi.org/10.5880/GFZ.2.1.2017.001>, (2017)
40. King, G. C. P., Stein, R. S. & Lin, J. Static stress changes and the triggering of earthquakes. *Bull. Seismol. Soc. Am.* **84**, 935-953 (1994).
41. Stein, R. S. The role of stress transfer in earthquake occurrence, *Nature* **402** (6762), 605–609 (1999).
42. Hainzl, S., Brietzke, G. B. & Zoeller, G. Quantitative earthquake forecasts resulting from static stress-triggering. *J. Geophys. Res.* **115**, B11311, doi: 10.1029/2010JB007473 (2010).
43. Richter, G., Hainzl, S., Dahm, T. & Zoeller, G. Stress-based, statistical modeling of the induced seismicity at the Groningen gas field, The Netherlands. *Environmental Earth Sciences* **79**, 252, doi: 10.1007/s12665-020-08941-4.
44. Beyerlee, J. Friction of rocks, *Pure and Applied Geophysics*, **116**, 615-626, (1978).
45. Dahm, T. On the shape and velocity of fluid-filled fractures in the Earth. *Geophys. J. Int.*, **142**, 181-192, (2000).
46. Gudnason et al. Seismic monitoring during drilling and stimulation of well RN-15/IDDP-2 in Reykjanes, SW-Iceland. *Proceedings World Geothermal Congress 2020+1*, (2021)

Figures

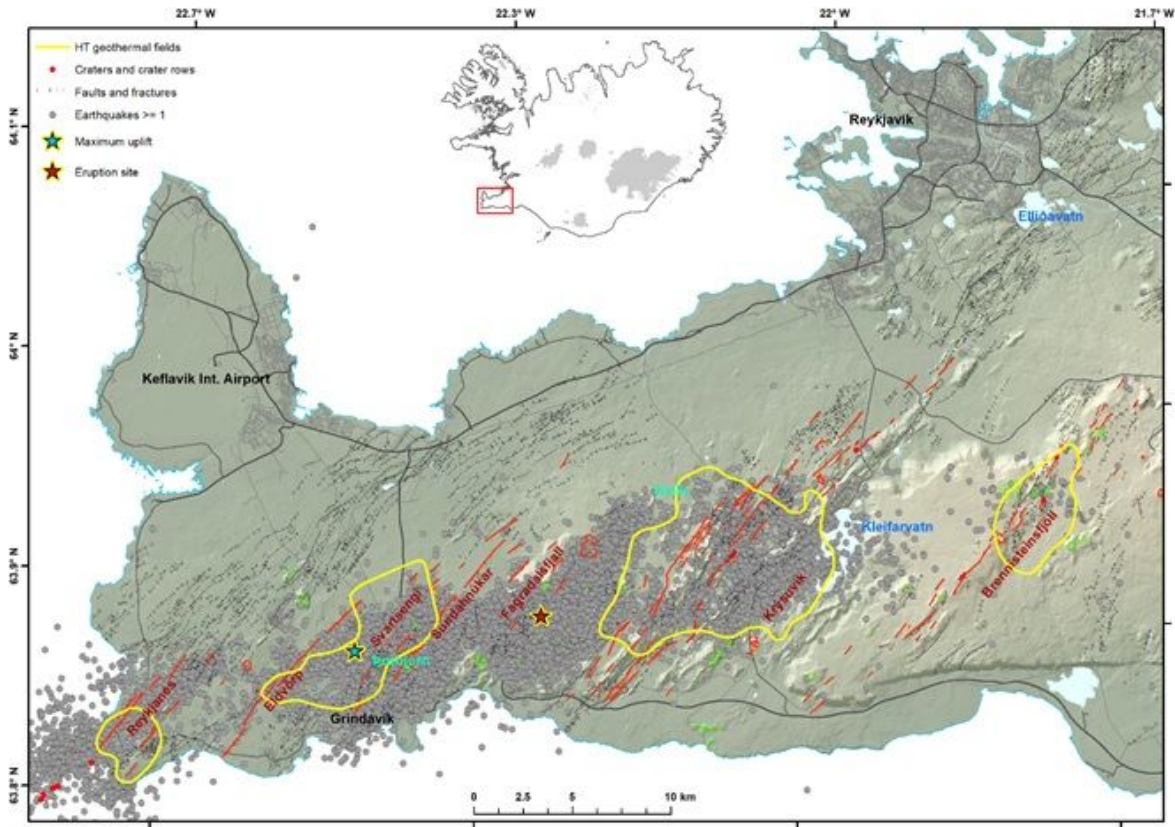


Figure 1

Overview of the geology of the Reykjanes Peninsula. The red and grey fault lines denote postglacial volcanic eruption fissures and opening fissures, respectively. Grey dots show the seismicity from September 2019 – May 2021. Yellow lines show the extent of the high-temperature geothermal fields on the peninsula, according to resistivity measurements. The blue and red stars show the centre of uplift and the 2021 eruption site, respectively. Continuous black lines show main roads, and topography is indicated as colored background. Main landmarks referenced in the text are shown on the map.

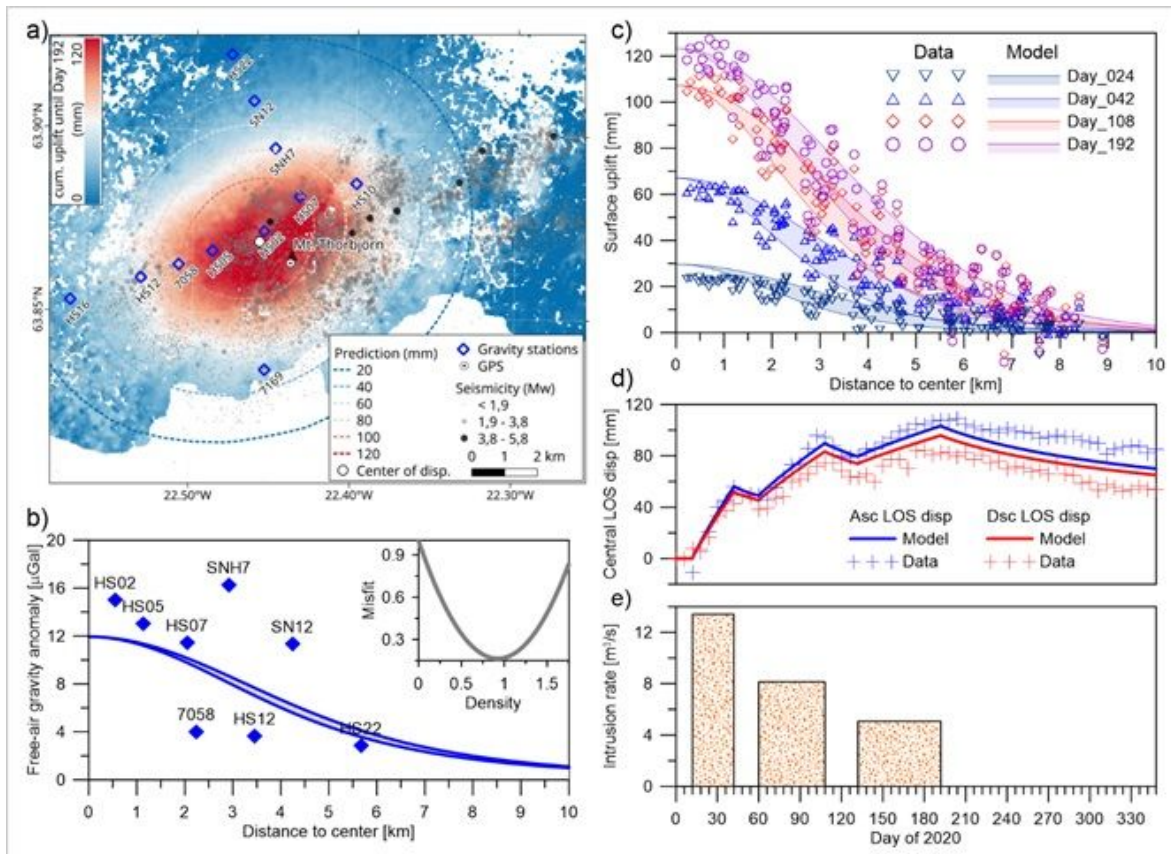


Figure 2

a. Maximum uplift displacement map relative to 17th July 2020 (Day 192); the vertical component was calculated from combining ascending and descending LOS displacements; the contour lines indicate the poroelastic linear modeled displacement field for the same date; blue diamonds show the location of the gravity stations; red circle shows the location of the centre of uplift obtained from Mogi source inversion; white with black dot circle shows the location of the GPS station used for the InSAR validation. Mount Thorbjörn position is indicated with a white triangle. Red triangle shows the location of the eruptive vents opened in March/April 2021. Earthquake epicenters are plotted in grey-scale dots. The dashed line shows the cross section profile in Fig. 4a. b. Free-air gravity anomalies (blue diamonds) from the campaign measurements between 27 January and 20 April 2020, compared with the model predictions (solid curves) along the major and minor axes of the elliptic uplift pattern. The inset figure shows the model-data misfit as a function of density of the intruded fluid, with the minimum at $0.836 \times 10^3 \text{ kg/m}^3$. c. Temporal snapshots of surface uplift derived from the InSAR data, compared with the model predictions. The double model curves for each snapshot show the values along the major and minor axes of the elliptic uplift pattern. d. Comparison between the predicted and measured ascending and descending LOS displacements at the pixel nearest to the uplift center. e. Fluid injection rates during the 3 surface uplift episodes estimated through the poroelastic modelling.

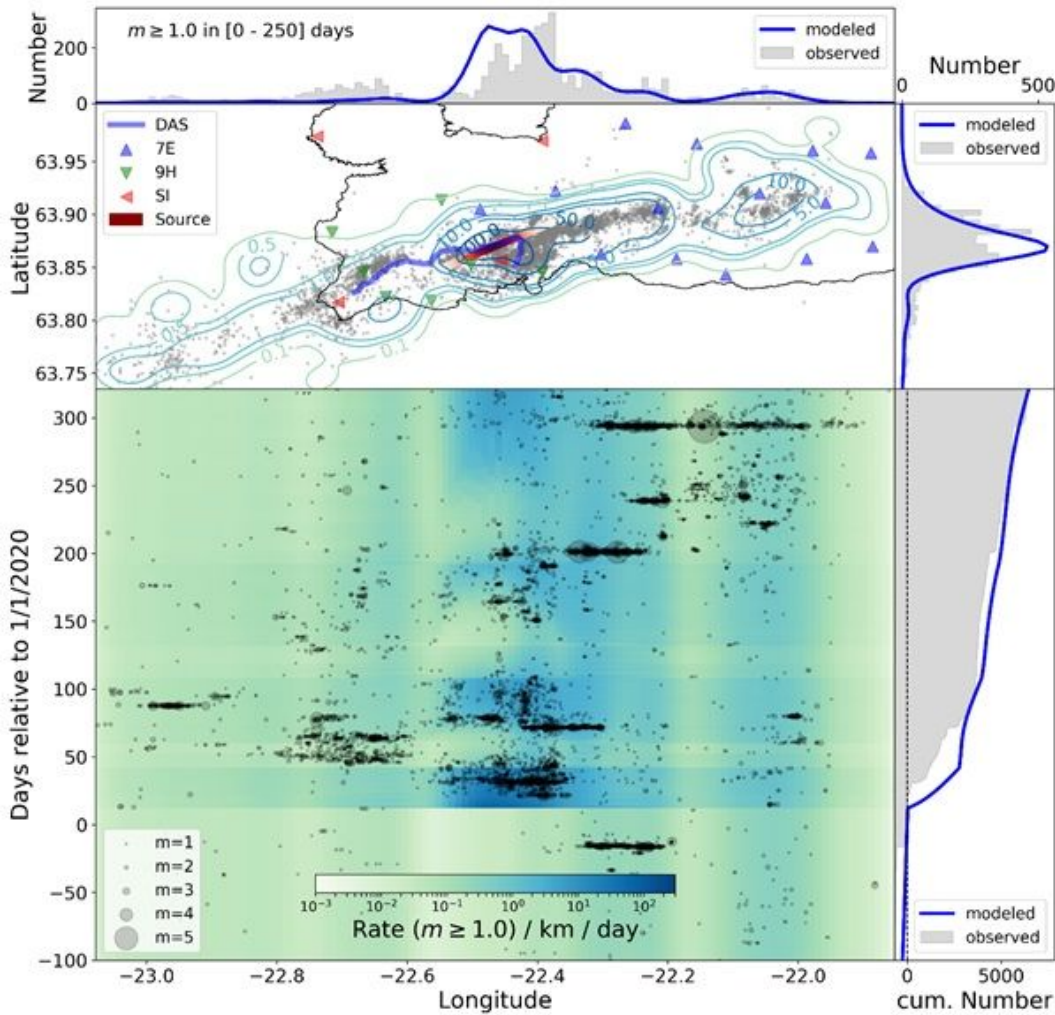


Figure 3

Comparison of observed $m \geq 1$ seismicity (grey/black) with model predictions (colored) based on induced crustal stress changes related to the geodetically inverted source model. The contour plot shows the numbers predicted per km^2 within the first 250 days of 2020, while points indicate the observed events for this period. Seismic stations are marked with triangles (7E=seismic network operated by the Institute of Geophysics, Academy of Sciences of the Czech Republic and ISOR, 9H=temporary seismic network operated by GFZ, SI=SIL seismic network operated by the Icelandic Met Office) and the DAS cable with a bold blue line. The corresponding cumulative numbers are shown as a function of longitude and latitude on the contour plot's top and right. The temporal evolution is compared in the bottom time-versus-longitude plot, where colors refer to the model's event density and magnitude-scaled points to observed earthquakes. The longitudinally integrated numbers are shown on the right.

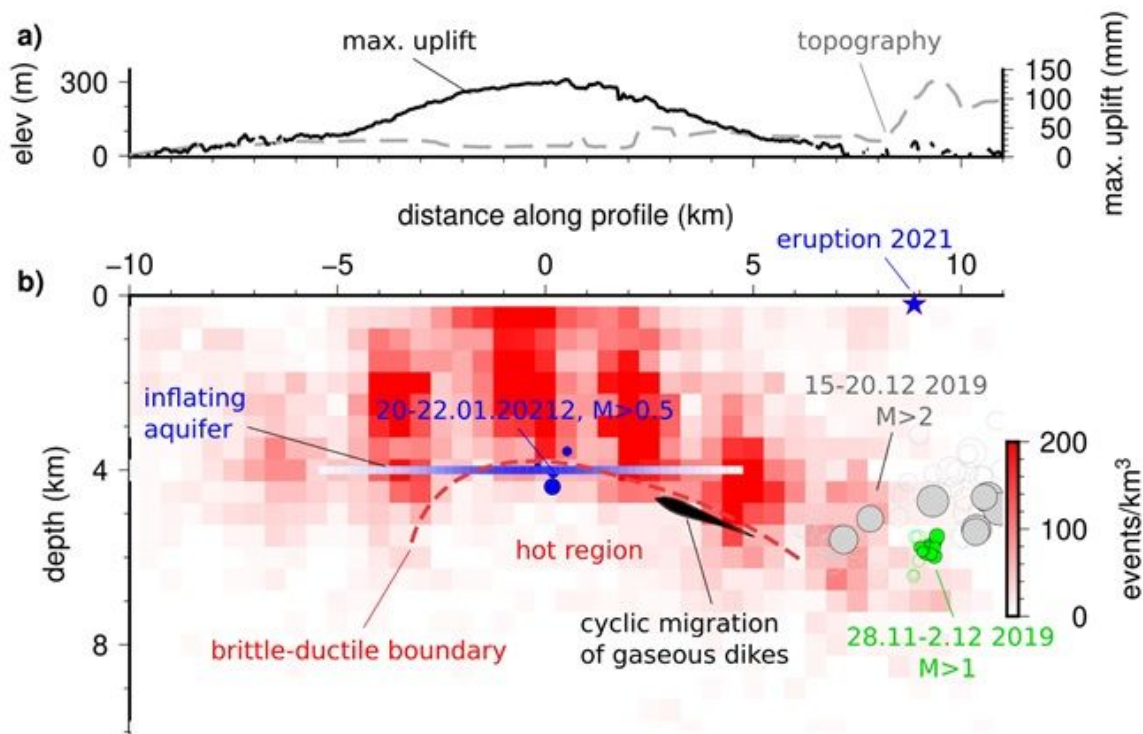


Figure 4

Sketch of fluid migration paths and aquifer location compared to observed seismicity and uplift. a. Maximum uplift (solid black line) and topography (dashed gray line) along the profile in Fig. 2a ($x=0$ at Mt. Thorbjörn). b. Density of own-located micro-earthquakes between February and August 2020 (gridded file and color scale) was estimated in a 1 km wide band along the profile. The inferred brittle-ductile boundary is indicated by the red dashed line. The manually relocated, largest events from the earthquake swarms from November (green circles) and December 2019 (gray circles) and at the beginning of unrest at Svartsengi (blue circles) are shown. The position and source intensity of aquifer model is indicated.

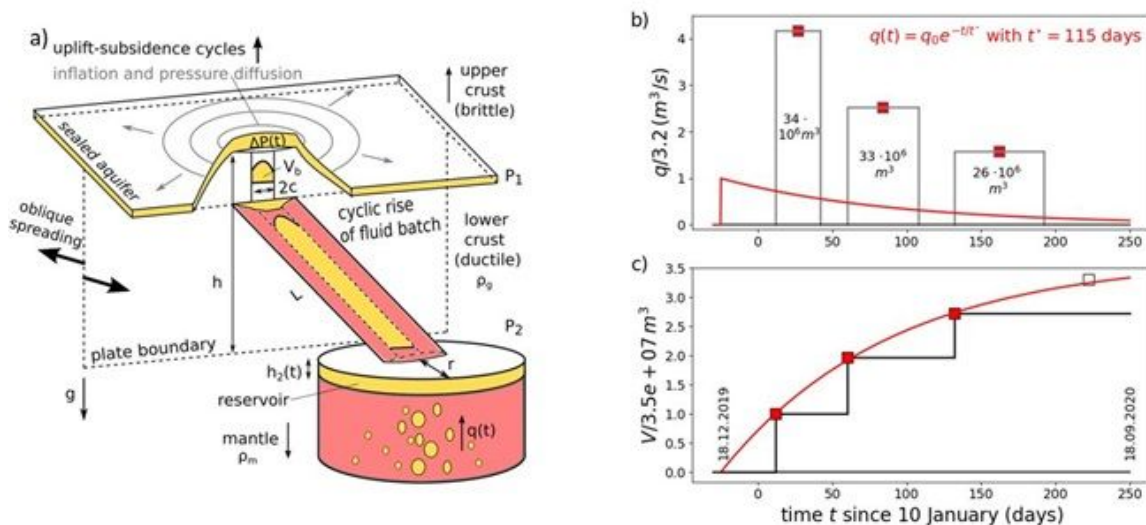


Figure 5

a. Sketch of the deep geodynamic structures and the assumed magmatic and fluid reservoir discontinuously pressurizing the aquifer at the plate boundary at 4 km depth. See method section for description of parameters and

more explanations. b. Model flow rate at entry point of transport channel (red line) to explain the time, duration and magnitude of injections at the aquifer level (black rectangulars). c. Time function of the predicted cumulative volume at the entry point of the discontinuous transport channel / fault (red solid line) is compared to the discontinuous volumes (black line) arriving at the aquifer level in 4 km depth. Red squares indicate the onset of the new batches of magmatic fluids. The open squares indicate the batch arriving at the Krýsuvík HT field in September 2020.

Supplementary Files

This is a list of supplementary files associated with this preprint. Click to download.

- [FlovenzetaSupplementmaterial.pdf](#)